

Robust training of implicit generative models for multivariate and heavy-tailed distributions with an invariant statistical loss.

José Manuel de Frutos^{a,*}, Manuel A. Vázquez^{a,b}, Pablo M. Olmos^{a,b}, Joaquín Míguez^{a,b}

^a*Departamento de Teoría de la Señal y Comunicaciones, Edificio Torres Quevedo, Escuela Politécnica Superior, Universidad Carlos III de Madrid, Av. de la Universidad, 30, Madrid, 28911, Spain*

^b*Instituto de Investigación Sanitaria Gregorio Marañón (IiSGM), Pabellón de Gobierno. Doctor Esquerdo, 46, Madrid, 28007, Spain*

Abstract

Traditional implicit generative models are capable of learning highly complex data distributions. However, their training involves distinguishing real data from synthetically generated data using adversarial discriminators, which can lead to unstable training dynamics and mode dropping issues. In this work, we build on the *invariant statistical loss* (ISL) method introduced in [1], and extend it to handle heavy-tailed and multivariate data distributions.

The data generated by many real-world phenomena can only be properly characterised using heavy-tailed probability distributions, and traditional implicit methods struggle to effectively capture their asymptotic behavior. To address this problem, we introduce a generator trained with ISL, that uses input noise from a generalised Pareto distribution (GPD). We refer to this generative scheme as Pareto-ISL for conciseness. Our experiments demonstrate that Pareto-ISL accurately models the tails of the distributions while still effectively capturing their central characteristics.

The original ISL function was conceived for 1D data sets. When the actual data is n -dimensional, a straightforward extension of the method was obtained by targeting the n marginal distributions of the data. This approach is computationally infeasible and ineffective in high-dimensional spaces. To overcome this, we extend the 1D approach using random projections and define a new loss function suited for multivariate data, keeping problems tractable by adjusting the number of projections. We assess its performance in multidimensional generative modeling and explore its potential as a pretraining technique for generative adversarial networks (GANs) to prevent mode collapse, reporting promising results and highlighting its robustness across various hyperparameter settings.

Keywords: implicit generative models, deep generative models, mode collapse, heavy-tailed distributions, multivariate distributions, random projections, time series forecasting

*Corresponding author

Email address: jofrutos@ing.uc3m.es (José Manuel de Frutos)

1. Introduction

1.1. Motivation

Probabilistic models can be divided into two primary types: prescribed models and implicit models [2]. Prescribed models give a parametric description of the distribution of an observed random variable (r.v.) x using a log-likelihood function $\log q_\theta(x)$, where θ denotes the parameters [3]. They include standard models in machine learning and statistics, such as classifiers for object recognition, sequence models for machine translation, and spatio-temporal models for disease spread [4, 5]. Implicit models, as highlighted by [6], directly generate data using a stochastic procedure, and are effective in areas like climate science, population genetics, and ecology [7, 8, 9, 10, 11].

Implicit generative models employ a neural network (NN) g_θ to convert a r.v. z drawn from a (known and typically simple) probability density function (pdf) p_z into a transformed variate $\tilde{y} = g_\theta(z)$ with pdf \tilde{p} . The objective is to select the set of parameters θ in such a way that the pdf \tilde{p} resembles a prescribed density p as much as possible. Specifically, the training process aims at minimising a discrepancy $d(p, \tilde{p})$, such that $d(p, \tilde{p}) = 0$ if and only if $p = \tilde{p}$.

In [1], a novel criterion was introduced to train univariate implicit methods, which simply requires checking the uniformity of a certain, easy-to-compute rank statistic. However, this new method has limitations. It is easy to see that a neural network trained with ISL and Gaussian input noise is unable to correctly model complex distributions such as heavy-tailed distributions.

Moreover, the method is limited to 1D scenarios. To address this limitation for multivariate time series, the authors in [1] proposed fitting marginals. However, this approach is problematic for high-dimensional data, as fitting each marginal can be intractable and does not guarantee convergence to the target distribution, since in many cases, marginal distributions fail to capture key dependencies in the data distribution.

1.2. Contributions

In this paper we aim at refining the theoretical analysis of the ISL method and then tackle its application to problems with heavy-tailed and multidimensional data distributions. Our main contributions are summarised below.

- We extend the analysis in [1] to establish a novel result on the continuity of the rank statistic with respect to (w.r.t.) the L^1 norm. We prove that if the L^1 norm of the difference between $p - \tilde{p}$ is bounded by $\epsilon > 0$, the difference between the probability mass function (pmf) of the rank statistic and the uniform discrete distribution is also bounded by ϵ . This generalises to any L^q norm, with $q \in [1, \infty]$, for pdfs p and \tilde{p} with compact support. We define a new theoretical loss function, proving its continuity and almost-everywhere differentiability, and show it can be optimised using a surrogate function, demonstrating numerically that the approximation error is negligible.

- We address the limitations of standard ISL in modeling heavy-tailed distributions by introducing a scheme termed Pareto-ISL, which incorporates a generalized Pareto distribution (GPD) as noise input. The generator, is explicitly designed to handle unbounded distributions and experiments show that it consistently outperforms other generative models in approximating both the central and tail regions of heavy-tailed distributions.
- Finally, we extend the ISL method to multivariate datasets using random projections and introduce a new loss function and algorithm, termed ISL-slicing, suitable for n -dimensional data. Through a series of experiments, we assess the ability of the method to generate multidimensional distributions with different topologies, as well as its effectiveness compared to other implicit schemes. In particular, we note improvements over the use of ISL to fit the n marginals of an n -dimensional data distribution as suggested in [1]. Additionally, we compare its performance to other state-of-the-art techniques in multivariate time series prediction. We show that ISL-slicing, especially when used as a pretraining method, is both effective and robust, consistently capturing the complete support of the target distribution across various hyperparameter settings.

1.3. Organization of the paper

In Section 2, we review the construction and key properties of the rank statistic introduced in [1] for completeness and then define the theoretical loss function and introduce a continuously differentiable surrogate loss function. Section 3 introduces the Pareto-ISL generative scheme for modeling heavy-tailed distributions. On the other hand, Section 4 evaluates the effectiveness of random projections in generating multidimensional distributions and their utility as a pretraining method, comparing them to other approaches for multivariate data distributions. The proposed techniques are exploited in Section 5 for time series prediction. Finally, Section 6 is devoted to conclusions.

2. Rank statistics and the invariant loss function

2.1. Discrete uniform rank statistics

Let $\tilde{y}_1, \dots, \tilde{y}_K$ be a random sample from a univariate real distribution with pdf \tilde{p} and let y be a single random sample independently drawn from another distribution with pdf p . We construct the set,

$$\mathcal{A}_K := \{\tilde{y} \in \{\tilde{y}_k\}_{k=1}^K : \tilde{y} \leq y\},$$

and the rank statistic

$$A_K := |\mathcal{A}_K|, \tag{1}$$

i.e., A_K is the number of elements in \mathcal{A}_K . The statistic A_K is a discrete r.v. that takes values in the set $\{0, \dots, K\}$; and we denote its pmf as $\mathbb{Q}_K : \{0, \dots, K\} \mapsto [0, 1]$. This pmf satisfies the following key result.

Theorem 1. *If $p = \tilde{p}$ then $\mathbb{Q}_K(n) = \frac{1}{K+1} \forall n \in \{0, \dots, K\}$, i.e., A_K is a discrete uniform r.v. on the set $\{0, \dots, K\}$.*

Proof. See [12] for an explicit proof. This is a basic result that appears under different forms in the literature, e.g., in [13] or [14]. \square

The following result generalises Theorem 2 in [1]. It establishes the continuity of the rank statistic w.r.t. the L^1 norm.

Theorem 2. *If $\|p - \tilde{p}\|_{L^1(\mathbb{R})} \leq \epsilon$ then,*

$$\frac{1}{K+1} - \epsilon \leq \mathbb{Q}_K(n) \leq \frac{1}{K+1} + \epsilon, \quad \forall n \in \{0, \dots, K\}.$$

Proof. See Appendix A. \square

Remark 1. *If p and \tilde{p} have compact support $\mathcal{K} \subset \mathbb{R}$, we can generalise the previous result. By Hölder's inequality [15, Theorem 4.6], we readily see that*

$$\|p - \tilde{p}\|_{L^1(\mathbb{R})} = \|\mathbb{I}_{\mathcal{K}}(p - \tilde{p})\|_{L^1(\mathbb{R})} \leq \|\mathbb{I}_{\mathcal{K}}\|_{L^q(\mathbb{R})} \|p - \tilde{p}\|_{L^{q'}(\mathbb{R})},$$

where $\frac{1}{q} + \frac{1}{q'} = 1$, $q \in [1, \infty]$, $\mathbb{I}_{\mathcal{K}}$ denotes the indicator function on \mathcal{K} , and $\|\mathbb{I}_{\mathcal{K}}\|_{L^q(\mathbb{R})} = \mathcal{L}(\mathcal{K})^{1/q}$, with $\mathcal{L}(\mathcal{K})$ being the Lebesgue measure of \mathcal{K} . Therefore, if $\|p - \tilde{p}\|_{L^{q'}(\mathbb{R})} \leq \epsilon / \mathcal{L}(\mathcal{K})^{1/q}$, then $\|p - \tilde{p}\|_{L^1(\mathbb{R})} \leq \epsilon$. This implies that Theorem 2 holds for any $L^{q'}$ with $q' \in [1, \infty]$ and not only for L^1 , provided that both p and \tilde{p} have compact support.

So far, we have shown that if the pdf of the generative model, \tilde{p} , is close to the target pdf, p , then the statistic A_K is close to uniform. A natural question to ask is whether A_K displaying a uniform distribution implies that $\tilde{p} = p$. This result is also established in [1] and is reproduced here for convenience.

Theorem 3. *Let p and \tilde{p} be pdf's of univariate real r.v.'s and let A_K be the rank statistic in Eq 1. If A_K has a discrete uniform distribution on $\{0, \dots, K\}$ for every $K \in \mathbb{N}$ then $p = \tilde{p}$ almost everywhere (a.e.).*

Remark 2. *If p and \tilde{p} are continuous functions then Theorem 3 implies that $p = \tilde{p}$ (everywhere).*

2.2. The invariant statistical loss function

In this subsection we build upon previous results to introduce a new discrepancy function $d_K(p, \tilde{p}) : C(\mathcal{K}) \times C(\mathcal{K}) \mapsto [0, +\infty)$ between two continuous densities on a compact set $\mathcal{K} \subset \mathbb{R}$. This function measures the ℓ_1 -norm of the difference between the pmf \mathbb{Q}_K associated with the statistic A_K and the uniform pmf, i.e.,

$$d_K(p, \tilde{p}) = \frac{1}{K+1} \left\| \frac{1}{K+1} \mathbf{1}_{K+1} - \mathbb{Q}_K \right\|_{\ell_1} = \frac{1}{K+1} \sum_{n=0}^K \left| \frac{1}{K+1} \mathbf{1}_{K+1} - \mathbb{Q}_K(n) \right|.$$

It is clear that $d_K(p, \tilde{p}) \geq 0$ for any pair of pdf's p and \tilde{p} . According to Theorem 2 and Theorem 3, for asymptotically large K , $d_K(p, \tilde{p}) = 0$ for arbitrarily large K if, and

only if, $p = \tilde{p}$. Thus, $\lim_{K \rightarrow \infty} d_K(p, \tilde{p})$ is a probability divergence [16, 17]. Furthermore, Theorem 2 states that if $\|p - \tilde{p}\|_{L^1(\mathbb{R})}$ then $d_K(p, \tilde{p}) \leq \epsilon$. This discrepancy measure serves as the theoretical loss function on which we build up a training procedure for implicit generative models.

The following theorem identifies two key regularity properties of the divergence $d_K(p, \tilde{p})$.

Theorem 4. *Let $p : X \rightarrow [0, \infty)$ be a pdf, where $X \subseteq \mathbb{R}$. Let Z be a real r.v. taking values in $\mathcal{Z} \subseteq \mathbb{R}$ and choose a function*

$$\begin{aligned} g : \mathcal{Z} \times \mathbb{R}^d &\rightarrow X, \\ (z, \theta) &\rightarrow g_\theta(z). \end{aligned}$$

Let \tilde{p}_θ denote the pdf of the r.v. $g_\theta(Z)$. Then,

1. *If g is continuous w.r.t. θ for almost every $x \in \mathcal{Z}$, then $d_K(p, \tilde{p}_\theta)$ is also continuous w.r.t. θ .*
2. *Assume that $g_\theta(z)$ satisfies the Lipschitz condition w.r.t. θ , i.e., $|g_\theta(z) - g_{\theta'}(z)| \leq L(z)\|\theta - \theta'\|$, and there is a constant $L_{\max} < +\infty$ such that $L(z) < L_{\max}$ for almost every $z \in \mathcal{Z}$. If $g_\theta(z)$ is differentiable w.r.t. z and there exists $m > 0$ such that $\inf_{(z, \theta) \in \mathcal{Z} \times \mathbb{R}^d} |g'_\theta(z)| \geq m > 0$, then $d_K(p, \tilde{p}_\theta)$ is Lipschitz continuous w.r.t. θ , and consequently, it is differentiable a.e.*

Proof. The proof of the Theorem can be found in Appendix B. □

Theorem 4 shows that the discrepancy $d_K(p, \tilde{p}_\theta)$, which measures the difference between a fixed density p and a parametric family \tilde{p}_θ generated by $g_\theta(z)$, is continuous whenever $g_\theta(z)$ is continuous in θ . Additionally, if g_θ is Lipschitz continuous and monotonic, the discrepancy becomes differentiable a.e. However, since the dependence of the empirical distribution \mathbb{Q}_K on θ is unknown, gradient-based methods cannot be directly use to minimise $d_K(p, \tilde{p}_\theta)$ w.r.t. θ .

2.3. The surrogate invariant statistical loss function

Since the divergence $d_K(p, \tilde{p}_\theta)$ cannot be used in practice, we present a surrogate loss function that is tractable, in the sense that it can be optimised w.r.t. the network parameters θ using standard methods. The training dataset consists of a set of N i.i.d. samples, y_1, \dots, y_N , from the true data distribution, p . For each y_n , we generate K i.i.d. samples from the generative model, denoted $\tilde{\mathbf{y}} = [\tilde{y}_1, \dots, \tilde{y}_K]^\top$, where $\tilde{y}_i = g_\theta(z_i)$. From \tilde{y}_i we obtain one sample of the r.v. A_K , that we denote as $a_{K,n}$.

We replace $d_K(p, \tilde{p}_\theta)$ by a differentiable approximation and refer to this surrogate function as invariant statistical loss (ISL) [1]. The ISL mimics the construction of a histogram from the statistics $a_{K,1}, a_{K,2}, \dots, a_{K,N}$. Given a real data point y_n , we can tally how many of the K simulated samples in $\tilde{\mathbf{y}}$ are less than the n -th observation y_n . Specifically, one computes

$$\tilde{a}_{K,n}(y) = \sum_{i=1}^K \sigma_\alpha(y_n - \tilde{y}_i) = \sum_{i=1}^K \sigma_\alpha(y_n - g_\theta(z_i)),$$

where $z_i \sim p_z$ is a sample from a univariate distribution, and $\sigma_\alpha(x) := \sigma(\alpha x)$, with $\sigma(x) := 1/(1 + \exp(-x))$ the sigmoid function. As we can see, $\tilde{a}_{K,n}$ is a differentiable (w.r.t. θ) approximation of the actual statistic A_K for the observation y_n . The parameter α enables us to adjust the slope of the sigmoid function to better approximate the (discrete) ‘counting’ in the construction of $\tilde{a}_{K,n}$.

A differentiable surrogate histogram is constructed from $\tilde{a}_{K,1}, \dots, \tilde{a}_{K,n}$ by leveraging a sequence of differentiable functions. These functions are designed to mimic the bins around $k \in \{0, \dots, K\}$, replacing sharp bin edges with functions that replicate bin values at k and smoothly decay outside the neighborhood of k . In our particular case, we consider radial basis function (RBF) kernels $\{\psi_k\}_{k=0}^K$ centered at $k \in \{0, \dots, K\}$ with length-scale ν^2 , i.e., $\psi_k(a) = \exp(-(a - k)^2/2\nu^2)$. Thus, the approximate normalized histogram count at bin k is given by

$$q[k] = \frac{1}{N} \sum_{i=1}^N \psi_k(\tilde{a}_{K,i}(y_i)), \quad (2)$$

for $k = 0, \dots, K$. The ISL is computed as the ℓ -norm distance between the uniform vector $\frac{1}{K+1} \mathbf{1}_{K+1}$ and the vector of empirical probabilities $\mathbf{q} = [q[0], q[1], \dots, q[K]]^\top$, namely,

$$\mathcal{L}_{ISL}(\theta, K) := \left\| \frac{1}{K+1} \mathbf{1}_{K+1} - \mathbf{q} \right\|_\ell. \quad (3)$$

Remark 3. *The ISL is a sum and composition of $C^\infty(\mathbb{R})$ functions. It is smooth w.r.t. the fictitious samples $\{\tilde{y}_i\}_{i=0}^K$ and the data y_n . As a result, its regularity aligns with that of the neural network (as a function of both its parameters and the input noise).*

The hyperparameters for the ISL method include the number of samples K , which is tunable, the activation function $\sigma(\alpha \cdot x)$, and the set of basis functions $\{\psi_k\}_{k=0}^K$, specified as radial basis function (RBF) kernels with a length scale of ν^2 . These parameters control the flexibility and behavior of the model during learning.

In Appendix C.1 we present a numerical study of the accuracy in the approximation of the divergence $d_k(p, \tilde{p}_\theta)$ by its surrogate, ISL \mathcal{L}_{ISL} .

2.4. Progressively training by increasing K

The training procedure can be made more efficient by performing it in a sequence of increasing values of K (see [1]). Specifically, one can select $K^{(1)} < K^{(2)} < \dots < K^{(I)}$, where I is the total number of stages and $K^{(I)} = K_{\max}$, the maximum admissible value of K . The iterative training scheme is outlined in Algorithm 1. The gain in efficiency of the progressive training procedure compared to a scheme with fixed K is illustrated in Appendix C.2.

3. Pareto-ISL

As shown in [1], ISL outperforms other generative methods in learning the central regions of typical 1D distributions. However, Figure 1 indicates that when standard

Algorithm 1 Progressively training by increasing K

- 1: **Input** Neural network g_θ ; hyperparameters N ; number of epochs; training data $\{y_i\}_{i=1}^N$; K_{\max} maximum admissible value of K .
 - 2: **Output** Trained neural network g_θ .
 - 3: $K = K^{(1)}$
 - 4: **For** $t = 1, \dots, \text{epochs}$ **do**
 - 5: Train g_θ using ISL loss function: $\mathcal{L}_{\text{ISL}}(\theta, K^{(t)})$
 - 6: Compute $\{a_{K^{(t)},1}, \dots, a_{K^{(t)},N}\}$
 - 7: Compute Pearson χ^2 test against $\mathbb{Q}_{K^{(t)}}$ using $\{a_{K^{(t)},1}, \dots, a_{K^{(t)},N}\}$
 - 8: **If** hypothesis " A_K is uniform" is accepted **and** $K^{(t)} < K_{\max}$ **do**
 - 9: Set $K = K^{(t+1)}$
 - 10: **return** g_θ
-

Gaussian noise is used as an input, NNs struggle to capture the tails of Cauchy mixtures, since compactly supported inputs cannot produce unbounded pdfs (which we will refer to as unbounded distributions). This issue can be addressed by using input noise from a generalized Pareto distribution (GPD). In this section, we introduce Pareto-ISL, which utilizes a GPD for input noise, and demonstrate its effectiveness in learning heavy-tailed distributions.

3.1. Tail distributions and extreme value theory

The conditional excess distribution function $F_u(y)$ provides a key tool for analyzing the tail of a distribution by focusing on exceedances over a specified threshold u . This function describes the probability distribution of the excess amount $X - u$, given $X > u$ exceeds u . By conditioning on large values, it isolates the behavior of the distribution in its tail, where extreme or rare events are more likely to occur. In the context of extreme value theory, for sufficiently high thresholds u , the conditional excess distribution function converges to the GPD. The GPD, parameterized by the tail index ξ and scaling parameter σ , provides a flexible model for the tail, allowing us to characterize its heaviness and the probability of extreme values.

The following definitions are taken from [18] and provided here for convenience.

Definition 1. *The conditional excess distribution function with threshold $u \in \mathbb{R}$ is defined as*

$$F_u(y) = \mathbb{P}(X - u \leq y | X > u) = \frac{F(u + y) - F(u)}{1 - F(u)}.$$

Definition 2. *The GPD, parametrized by tail index $\xi \in \mathbb{R}$ and scaling parameter $\sigma \in \mathbb{R}^+$, has the following complementary cumulative distribution function (CCDF)*

$$S(z; \xi, \sigma) = \begin{cases} (1 + \xi z / \sigma)^{-1/\xi}, & \text{for } \xi \neq 0, \\ e^{-z/\sigma}, & \text{for } \xi = 0. \end{cases}$$

Lipschitz continuous functions map bounded distributions to bounded ones [19, Chapter 3], limiting the ability of NNs to model heavy-tailed distributions. To address this, unbounded input distributions and NN generators are required.

To construct unbounded NN generators, recall that piecewise linear (PWL) functions, (which include operations like rectified linear unit (ReLU), leaky ReLU, linear layers, addition, and batch normalization), are closed under composition [20, Theorem 2.1] and are unbounded, making them ideal for constructing generators that approximate heavy-tailed distributions. We then define a Pareto-ISL generator, g^{PWL} , as a piecewise linear generator driven by an input from a GPD with tail index ξ , and trained using ISL. Estimators such as Hill’s estimator [21] can be used to estimate ξ , aiding in the accurate modeling of heavy-tailed behavior.

Definition 3 (Pareto-ISL). *Let $z_\xi = (U^{-\xi} - 1)/\xi$, where $U \sim \mathcal{U}(0, 1)$, be a GPD r.v. with tail index ξ and CCDF $S(x; \xi, 1)$. A Pareto-ISL generator is g^{PWL} , with an input distribution z_ξ parameterized by ξ , and output distribution $x_\xi = g_\theta^{PWL}(z_\xi)$.*

The Pickands-Balkema-de Haan theorem [22] states that for a wide range of probability distributions, the conditional excess distribution function converges to the GPD as the threshold u increases. This applies to distributions like Gaussian, Laplacian, Cauchy, Lévy, Student-t, and Pareto. Building on this result and [18, Theorem 2], a generator constructed using g^{PWL} with a GPD input can effectively approximate the conditional excess distribution of heavy-tailed distributions. Specifically, if x_ξ has unbounded support, the conditional excess distribution $F_u(x)$ of x_ξ converges to $S(x; \xi, \sigma)$ for some $\sigma \in \mathbb{R}^+$. This indicates that ISL-Pareto is especially well-suited for these types of problems, outperforming other implicit methods, including ISL with non-Pareto noise, as we demonstrate in the following subsection.

3.2. Comparison of Pareto-ISL and standard ISL in learning a Cauchy mixture

In Figure 1, we compare Pareto-ISL against standard ISL where the data distribution is a two-component Cauchy mixture with locations at -1.0 and 1.0 , and scales 0.7 and 0.85 . All generators use a uniform four-layer multilayer perceptron (MLP) with 35 units per layer and ReLU activation. Generators are trained with ISL using $K = 20$, $N = 1000$, and a learning rate of 10^{-3} . For Pareto-ISL, the tail parameter is set to $\xi = 1$, aligning GPD noise with the tail index of the Cauchy mixture. Introducing GPD noise improves tail approximation and enhances the modeling of the central part of the target distribution, as demonstrated in the logarithmic-scale (bottom row) and linear-scale (top row) of Figure 1.

In Appendix C.3, we present a multidimensional heavy-tailed distribution and compare Pareto-ISL to ISL with Gaussian noise (results shown in Figure C.9).

3.3. Performance evaluation of Pareto-ISL compared to other implicit generative models

In a second experiment, we evaluate the performance of Pareto-ISL as compared to different GANs. For this comparison, we consider four data distributions, including a Cauchy distribution with location parameter 1 and scale parameter 2 (labeled Cauchy(1, 2)), a Pareto distribution with scale parameter 1 and shape parameter 1 (labeled Pareto(1, 1)) and two mixture distributions, labeled Model₃ and Model₄. Model₃

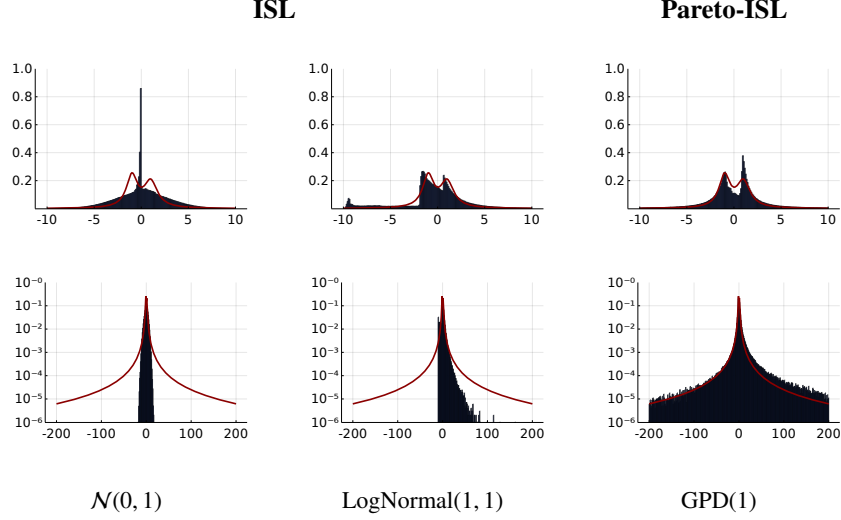


Figure 1: Pdfs approximated by generators with various tail behaviors. The noise input for each subplot is given by the subcaption of the corresponding column. Generators are trained on a mixture of Cauchy distributions, with the true density displayed in red. The top row presents the central region of the distributions on a linear scale, while the bottom row highlights the tails on a logarithmic scale.

is a mixture of a $\mathcal{N}(-5, 2)$ distribution and a $\text{Pareto}(5, 1)$ distribution, while Model_4 is a mixture of a $\text{Cauchy}(-1, 0.7)$ distribution and a $\text{Cauchy}(1, 0.85)$ distribution.

As generator NN, we use a 4-layer MLP with 7, 13, 7 and 1 units at the corresponding layers. As activation function we use a ReLU. We train each setting up to 10^4 epochs with 10^{-2} learning rate using Adam. We compare Pareto-ISL, GAN, Wasserstein GAN (WGAN) [23], and maximum mean discrepancy GAN (MMD-GAN) [24] using KSD (Kolmogorov-Smirnov distance), MAE (mean absolute error), and MSE (mean squared error) error metrics, defined as follows

$$\begin{aligned} \text{KSD} &= \sup_x |F(x) - \tilde{F}(x)|, \\ \text{MAE} &= \int_{\mathbb{R}} |g(z) - g_{\theta}(z)| p_z(z) dz, \\ \text{MSE} &= \int_{\mathbb{R}} (g(z) - g_{\theta}(z))^2 p_z(z) dz, \end{aligned}$$

where F and \tilde{F} represent, respectively, the cdfs of the data distribution and the r.v. generated by the neural network g_{θ} with input $z \sim p_z$. Moreover, g denotes the optimal transformation of the data distribution. The results are detailed in Table 1.

3.4. Assessment of Pareto-ISL on heavy-tailed datasets

In this third experiment, we demonstrate the effectiveness of the Pareto-ISL scheme on two univariate heavy-tailed datasets:

	Pareto-ISL			GAN			WGAN			MMD-GAN		
Target	KSD	MAE	MSE	KSD	MAE	MSE	KSD	MAE	MSE	KSD	MAE	MSE
Cauchy(1, 2)	1.90e⁻³	1.418	15.782	0.082	8.963	8207	0.030	10.568	8127	0.026	9.680	57975
Pareto(1, 1)	5.30e⁻³	1.155	2.409	0.099	12.640	114970	0.492	7.644	7062	0.501	9.023	10674
Model ₃	0.024	0.471	0.325	0.185	0.445	1.605	0.299	3.038	13.126	0.561	3.205	21.524
Model ₄	0.010	0.609	1.051	0.018	0.768	2.746	0.025	2.631	66.055	0.016	0.663	2.599

Table 1: Comparison of Pareto-ISL results with vanilla GAN, WGAN, and MMD-GAN when input noise is a standard Gaussian, $K_{max} = 10$, epochs = 1000, and $N = 1000$. The best result for each metric is highlighted in bold face.

- 136 million keystrokes (Keystrokes): this dataset includes inter-arrival times between keystrokes for a variety of users.
- Wikipedia web traffic (Wiki Traffic): this dataset includes the daily number of views of Wikipedia articles during 2015 and 2016.

Our assessment uses two metrics. First, we compute the KSD to compare the data distribution and the generated distribution. Then, we calculate the area A_{CCDF} between the log-log plots of the CCDFs of data and generated samples, indicating how well the tails of the distributions match. For n real samples, we have

$$A_{CCDF} = \sum_{i=1}^n \left[\log \left(F_p^{-1} \left(\frac{i}{n} \right) \right) - \log \left(\tilde{F}_{\tilde{p}}^{-1} \left(\frac{i}{n} \right) \right) \right] \log \left(\frac{i+1}{i} \right),$$

where F_p^{-1} and $\tilde{F}_{\tilde{p}}^{-1}$ are the inverse empirical CCDFs for the data distribution p and the generated distribution \tilde{p} , respectively.

We use a common network architecture and training procedure for all experiments. The network consists of 4 fully connected layers with 32 hidden units per layer and ReLU activations. Results are shown in Table 2.

Methods	Keystrokes		Wiki Traffic	
	KS	A_{CCDF}	KS	A_{CCDF}
Uniform (ISL)	0.087	6.2	0.025	10.3
Normal (ISL)	0.090	2.7	0.023	8.6
Lognormal (ISL)	0.096	1.7	0.019	9.5
Pareto GAN [18]	0.013	21.1	0.017	4.5
Pareto-ISL	0.006	1.4	0.017	1.19

Table 2: Pareto-ISL outperforms ISL baselines and Pareto GAN [18] on tail estimation across the two datasets, while maintaining a better or, at least comparable KS performance.

4. ISL-Slicing: A Random Projections-Based Approach

Machine learning datasets are often multi-dimensional. Building on [25, 26], we extend the one-dimensional loss function \mathcal{L}_{ISL} to a general metric for higher dimensions.

We do this by randomly projecting high-dimensional data onto various 1D subspaces, specifically in all possible directions $s \in \mathbb{S}^d$, where \mathbb{S}^d is the unit hypersphere in $d + 1$ -dimensional space.

Let x be a $(d + 1)$ -dimensional r.v. and let $s \in \mathbb{R}^{d+1}$ be a deterministic vector. We denote by $s\#p$ the pdf of the real r.v. $y = s^\top x$. Using this notation we define the *sliced ISL distance* between distributions with pdfs p and \tilde{p} as

$$d_K^{\mathbb{S}^d}(p, \tilde{p}) := \int_{s \in \mathbb{S}^d} d_K^s(p, \tilde{p}) ds,$$

where $d_K^s(p, \tilde{p}) = d_K(s\#p, s\#\tilde{p})$.

Since the expectation in the definition of the sliced ISL distance is computationally intractable, we approximate it using Monte Carlo sampling. Specifically, we choose a pdf q on \mathbb{S}^d and sample directions $s_i \sim q$, for $i = 1, \dots, m$. Then, the Monte Carlo approximation of the sliced ISL distance is

$$\tilde{d}_K^{\mathbb{S}^d}(p, \tilde{p}) = \frac{1}{m} \sum_{i=1}^m d_K(s_i\#p, s_i\#\tilde{p}). \quad (4)$$

If $\tilde{p} \equiv \tilde{p}_\theta$ is the pdf of the r.v. $y = g_\theta(z)$, $z \sim p_z$, i.e., the output of a NN with random input z and parameters θ , then one can use $\tilde{d}_K^s(p, \tilde{p}_\theta)$ as a loss function to train the NN.

Remark 4. In practice, we use the surrogate loss (see Section 2.3) to approximate $d_K(s_i\#p, s_i\#\tilde{p}_\theta)$ in Eq. 4, and sample random vectors from the unit sphere. Randomly chosen vectors from the unit sphere in a high-dimensional space are typically almost orthogonal. More precisely, ([27])

$$\mathbb{P}\left(\left|\frac{v_1^\top v_0}{\|v_1\|_2 \|v_0\|_2}\right| < \epsilon\right) > 1 - 2e^{-\frac{1}{2}d\epsilon^2},$$

where v_0 and v_1 are uniformly distributed random vectors, and ϵ is a small positive constant.

The pseudocode for training implicit models using the proposed random projection method, referred to as the *ISL-slicing algorithm*, is provided in Algorithm 2.

4.1. Random projections vs. marginals on high-dimensional data

Following [28], we conduct experiments on a multi-modal synthetic dataset. Specifically, we generate D -dimensional synthetic data from the model

$$\begin{cases} z \sim \mathcal{N}(0, 10 \cdot I_d), & A \sim \mathcal{N}(0, I_{D \times d}), & \epsilon \sim \mathcal{N}(0, 0.01 \cdot I_D), \\ x = Az + \epsilon, & d \ll D. \end{cases}$$

In these experiments, we fit a standard GAN to a dataset where $D = 100$ and $d = 2$. The generator is a 3-layer fully connected neural network with 10, 1000, and 100 units, respectively, using ReLU activations throughout.

Algorithm 2 ISL-slicing algorithm

```
1: Input Neural network  $g_\theta$ ; hyperparameter  $K$ ; number of epochs  $N$ ; batch size  $M$ ;
   training data  $\{y_i\}_{i=1}^N$ ; number of randomly chosen projections  $m$ .
2: Output Trained neural network  $g_\theta$ .
3: For  $t = 1, \dots, \text{epochs}$  do
4:   For iteration =  $1, \dots, N/M$  do
5:      $L = 0$ 
6:     Sample uniformly distributed random projection directions  $\hat{\mathbb{S}}^d = \{s_{1:m}\}$ 
7:     Select  $M$  samples from  $\{y_j\}_{j=1}^N$  at random
8:     For each  $s \in \hat{\mathbb{S}}^d$  do
9:        $\{z_i\}_{i=1}^K \sim \mathcal{N}(\mathbf{0}, I)$ 
10:       $\mathbf{q} = \frac{1}{M} \sum_{j=1}^M \psi_k \left( \sum_{i=1}^K \sigma_\alpha(s^\top y_j - s^\top g_\theta(z_i)) \right)$ 
11:       $L \leftarrow L + \nabla_\theta \left\| \frac{1}{K+1} \mathbf{1}_{K+1} - \mathbf{q} \right\|_2$ 
12:    Backpropagation( $g_\theta, \nabla_\theta L / m$ )
13: return  $g_\theta$ 
```

Figure 2 illustrates the performance of random projections (ISL-slicing) with the marginal pdf-based method from [1]. Our results show that even with a limited number of projections, ISL-slicing achieves a lower Jensen-Shannon divergence (JS-Divergence) w.r.t. the true distribution, as estimated by kernel density. This approach also significantly reduces computation time per iteration compared to ISL marginals, since the number of projections is a fraction of the total marginals. Specifically, it took 10x and 5x less execution time, respectively, to obtain the results shown in Figures 2a and 2b using the slicing method compared to the marginals method.

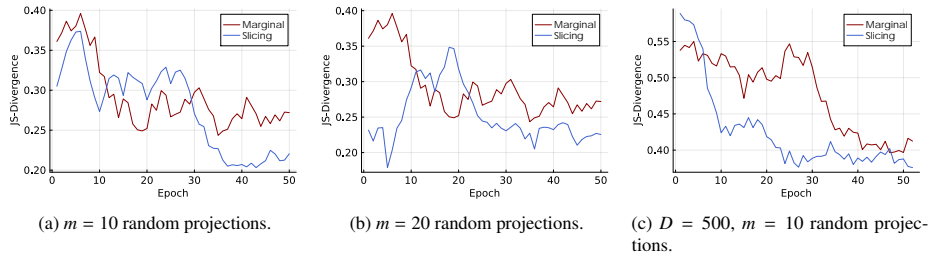


Figure 2: Performance evaluation of ISL-slicing vs ISL marginal methods on a synthetic dataset. Plots (a) and (b) correspond to $D = 100$ with different random projections ($m = 10$ and $m = 20$). Plot (c) corresponds to $D = 500$ and $m = 10$. The hyperparameters are $K = 10$, $N = 1000$ and learning rate $= 10^{-4}$.

4.2. Experiments on 2D distributions

We begin by examining simple 2D distributions characterized by different topological structures: one distribution with two modes, another with eight modes, and

a third featuring two rings. Our objective is to assess the ability of the ISL-slicing method to fully capture the support of these distributions. We compare our approach to normalizing flows and GANs, using KL-divergence and visual assessment as metrics.

For GAN, WGAN, and ISL, we use a 4-layer MLP generator with a 2D input sampled from a standard normal distribution. Each layer has 32 units and uses the hyperbolic tangent activation. The discriminator is an MLP with 128 units per layer, using ReLU activations except for the final sigmoid layer. We used a batch size of 1000 and optimized the critic-to-generator update ratio over $\{1:1, 2:1, 3:1, 4:1, 5:1\}$ for GAN and WGAN. The learning rate was chosen from $\{10^{-2}, 10^{-3}, 10^{-4}, 10^{-5}\}$. For ISL, we set $K = 10$, $N = 1000$, 10 random projections, and a learning rate of 10^{-3} . For the normalizing flow model, we used the RealNVP architecture from [29], with 4 layers of affine coupling blocks, parameterized by MLPs with two hidden layers of 32 units each. The learning rate was set to $5 \cdot 10^{-5}$, using the implementation from [30]. All methods were trained for 1000 epochs, with optimization performed using the ADAM algorithm.

Figure 3 highlights the challenges of training GANs, particularly their susceptibility to mode collapse. In contrast, normalizing flow methods preserve topology via invertibility constraints but struggle to model complex structures, often forming a single connected component due to density filaments. Our method overcomes this by capturing the full distribution support and distinguishing between connected components, as seen in the `Dual Moon` example. However, ISL can fill regions between modes, as seen in the `Circle of Gaussians`, an issue mitigated by increasing K . Alternatively, combining a pretrained network with ISL (trained for 100 epochs) and a GAN yielded the best results (method denoted as ISL+GAN), capturing full support while excluding zero-density regions. This approach is detailed further in Section 4.3. We also estimate the KL-divergences between the target and model distributions, as listed in Table 3. In all cases, the ISL method, and particularly the ISL+GAN approach, outperform the respective baselines.

Method / Dataset	Real NVP	GAN	WGAN	ISL	ISL+GAN
Dual moon	1.77	1.23	1.02	0.43	0.30
Circle of Gaussians	2.59	2.24	2.38	1.61	0.46
Two rings	2.69	1.46	2.74	0.56	0.38

Table 3: Performance comparison of generative methods on 2D distributions. The table summarizes KL-divergence results for Real NVP, GAN, WGAN, and ISL on `Dual Moon`, `Circle of Gaussians`, and `Two Rings`. Lower values indicate better performance.

4.3. ISL-pretrained GANs for robust mode coverage in 2D grids

In this experiment, we explore how ISL-pretrained GANs improve mode coverage on the 2D-Ring and 2D-Grid datasets, benchmarks commonly used in generative model evaluation. The 2D-Ring dataset consists of eight Gaussian distributions arranged in a circle, while the 2D-Grid dataset has twenty-five Gaussians on a grid. We first pretrain with ISL-slicing to ensure comprehensive mode coverage, then fine-tune with a GAN. Performance was compared to other GANs using two metrics: the number of covered modes (`#modes`) and the percentage of high-quality samples (`%HQ`). A mode is covered

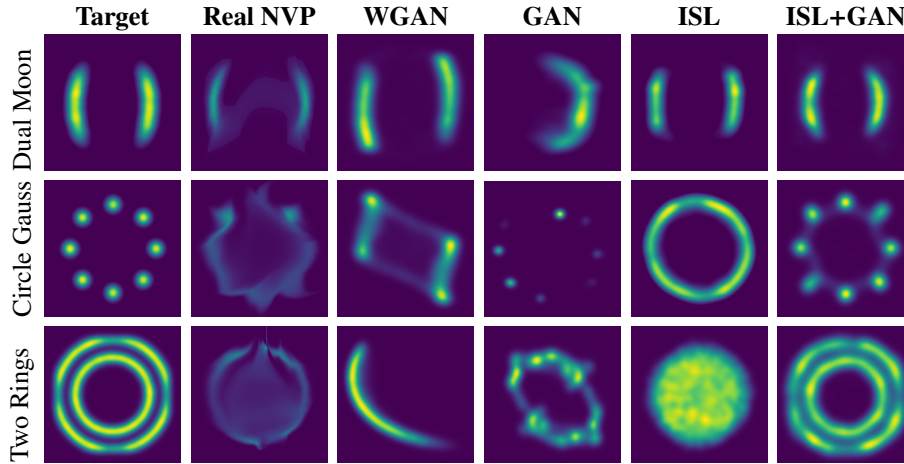


Figure 3: Comparison of the performance of various generative methods—Real NVP, WGAN, GAN, ISL-slicing, and GAN pretrained with ISL to approximate three complex 2D distributions: Dual Moon, Circle of Gaussians (referred to as Circle Gauss), and Two Rings. For a detailed description of the dataset, refer to [30]. The first column shows the target distributions, while the subsequent columns display the results generated by Real NVP, WGAN, GAN, ISL-slicing, and GAN pretrained with ISL, in that order.

if generated samples fall within three standard deviations of the Gaussian center, which also defines high-quality samples. The second metric represents their proportion among all generated samples.

We follow the experimental settings for GAN and WGAN as outlined by [31]. The generator is a 4-layer MLP with 128 units per layer and ReLU activation, while the discriminator is an MLP with 128 units, using ReLU except for a sigmoid in the final layer. We use a batch size of 128, a 1:1 critic-to-generator update ratio, and learning rates of 10^{-4} for GAN and 10^{-5} for WGAN, both optimized using ADAM. ISL was run for 250 epochs with $K = 10$, $N = 1000$, and 5 random projections, capturing the full support of the distribution. The GAN is then trained for 30000 epochs. The results presented in Table 4 and Figure 4 compare our method with other techniques for addressing mode collapse in GANs. They demonstrate that our approach performs on par with more advanced methods, such as DynGAN (a semi-supervised technique, see [31]) and BourGAN (computationally intensive, see [32]), while offering greater simplicity.

Finally, we conduct a robustness experiment comparing the performance of a WGAN with suboptimal hyperparameters to the same WGAN after ISL pretraining. Both use the same generator and discriminator architectures described in Section 4.2. The WGAN hyperparameters include a batch size of 1000, a critic-to-generator update ratio optimized over $\{1 : 1, 2 : 1, 3 : 1, 4 : 1, 5 : 1\}$, and a learning rate of 10^{-5} . For ISL, we use $K = 10$, $N = 1000$, 10 random projections, and a learning rate of 10^{-3} . Numerical results are displayed in Table 5. Additional experiments with batch sizes $\{64, 128, 252, 512\}$ and optimized critic-to-generator ratios are shown in Table 6. ISL-pretrained WGAN consistently outperforms standard WGAN across all ratios and batch

sizes, detecting all 8 modes and producing high-quality samples. This shows that ISL pretraining significantly enhances stability and performance, leading to more robust GAN training. Once all modes are captured by ISL, a low learning rate allows the generator to improve high-quality metrics while maintaining full distribution coverage.

Methods	2D-Ring		2D-Grid	
	#modes	%HQ	#modes	%HQ
GAN [33]	6.3	98.2	17.1	92.5
VEEGAN [34]	8.0	86.8	24.4	74.2
Pointwise [35]	8.0	87.5	25.0	76.7
BourGAN [32]	8.0	99.9	25.0	94.9
WGAN [23]	7.7	86.4	24.8	83.7
DynGAN- [31]	8.0	97.5	25.0	84.3
DynGAN [31]	8.0	99.5	25.0	96.0
ISL + GAN	8.0	97.9	24.6	96.8
ISL + WGAN	8.0	97.4	25.0	96.0

Table 4: Quantitative results on synthetic datasets. %HQ represents the percentage of high-quality samples, averaged over ten trials.

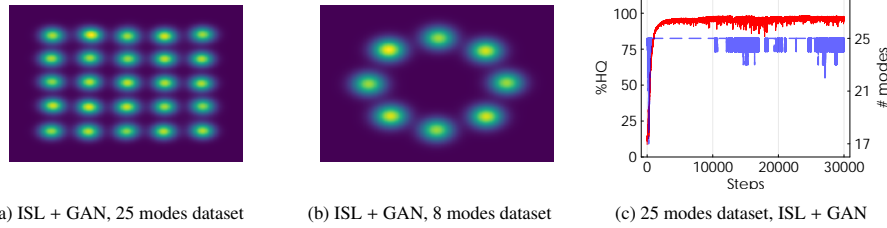


Figure 4: ISL + GAN on 25 and 8 modes datasets (plots (a) and (b)) with $K = 10$, $N = 1000$, ISL learning rate of 10^{-3} for 250 epochs, and GAN with a batch size of 128, 1:1 critic-generator ratio, and learning rate of 10^{-4} for 30000 epochs. Plot (c) shows the coverage of the 2D-Grid dataset, highlighting the number of modes covered (#modes, blue) and high-quality samples (%HQ, red) during GAN training after ISL pretraining.

Critics	WGAN			ISL + WGAN		
	#modes	%HQ	KL-div	#modes	%HQ	KL-div
1 : 1	3.7	40.99	33.99	8.0	97.74	0.51
1 : 2	7.0	0.07	59.58	8.0	98.43	0.47
1 : 3	8.0	0.63	57.05	8.0	97.39	0.55
1 : 4	8.0	0.44	59.18	8.0	98.07	0.78
1 : 5	8.0	0.19	56.83	8.0	98.24	0.72

Table 5: Comparison of WGAN and ISL + WGAN on the 2D-Ring dataset.

Batch Size	WGAN			ISL + WGAN		
	#modes	%HQ	KL-div	#modes	%HQ	KL-div
64	6.1	30.01	40.52	8.0	99.31	0.82
128	4.5	19.94	47.29	8.0	98.22	1.20
252	3.1	19.98	46.57	8.0	89.70	2.24
512	3.5	29.97	41.19	8.0	95.18	1.71

Table 6: Comparison of WGAN and ISL + WGAN with different batch sizes.

4.4. Preventing mode collapse in DCGANs on MNIST

We evaluate the ability of our method, in combination with DCGAN [36], to mitigate mode collapse on the MNIST dataset. The experiments begin by training the DCGAN with the hyperparameters in Table 7. After training, we generate 1000 digit images and used a pre-trained classifier to evaluate the digit distribution, expecting it to be

Hyperparameter DCGAN	Value
Batch size	128
Latent dimension	100
Epochs	10^4
Learning rate discriminator	10^{-5}
Learning rate generator	10^{-5}

Hyperparameter ISL	Value
K	10
N	1000
m	10
Epochs	600
Learning rate	0.001

Table 7: Hyperparameters for the DCGAN and ISL methods.

uniform. We repeated the process, this time with ISL pre-training (hyperparameters also in Table 7) followed by DCGAN training (ISL+DCGAN). A Kolmogorov-Smirnov test confirms the digit distribution was uniform with ISL+DCGAN, unlike DCGAN alone. For example, Figure 5 shows the digit distribution across 1000 generated images. The average p-values from the Kolmogorov-Smirnov test significantly improve with ISL+DCGAN ($p = 0.642$) versus DCGAN alone ($p = 0.010$), based on tests with 100 images, each containing 1000 digits. Figure 6 visually compares the MNIST samples: the left plot shows DCGAN-generated images, and the right plot those generated with ISL pre-training. In the latter, we observe a more evenly distributed appearance of digits.

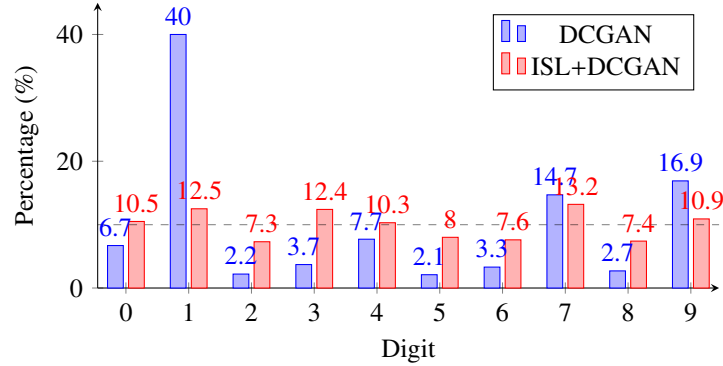


Figure 5: Digit distribution for DCGAN and ISL+DCGAN. Dashed line showing the 10% threshold.



(a) DCGAN



(b) DCGAN pretrained with ISL

Figure 6: Generated samples from the MNIST dataset: plot 6a shows numbers generated by a DCGAN, while the plot 6b shows numbers generated by a DCGAN pretrained with ISL.

5. Time series prediction

Our approach applies to both univariate and multivariate time series. Hereafter we briefly describe the methodology for both types for series and conclude the section with experiments comparing these techniques on various datasets.

5.1. Univariate time series prediction

Let $y[0], y[1], \dots, y[T]$ represent a realization of a discrete-time random process. We assume the process begins at $t = 0$, $Y[t]$ denotes the r.v. at time t , and $p_t = p(Y[t]|Y[0], \dots, Y[t-1])$ is the unknown conditional distribution. Given the sequence $y[0], y[1], \dots, y[t-1]$, we aim to train an autoregressive conditional implicit generator network, $g_\theta(z_t, \mathbf{h}[t])$, to approximate p_t . Here, z_t is a sequence of i.i.d. Gaussian r.v.s, and $\mathbf{h}[t]$ is an embedding of the sequence $y[0], \dots, y[t-1]$ via a NN, such as a simple RNN connected to the generator (see Figure 7). At time t , the observation $y[t]$ is fed into the RNN, compressing the history into a hidden state $\mathbf{h}[t]$. The generator $g_\theta(z, \mathbf{h}[t])$ uses this hidden state and noise z to predict $\tilde{y}[t+1]$. During testing, $\tilde{y}[t+1]$ is fed back into the RNN for forecasting.

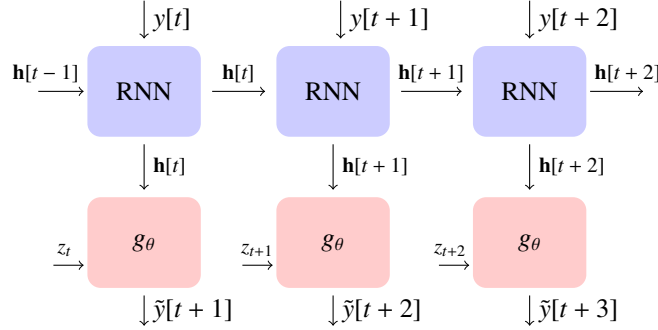


Figure 7: Conditional implicit generative model for time-series prediction.

As noted in [1], all results from previous sections remain valid in this temporal setup. The sequence of observations $\mathbf{y} = [y[0], y[1], \dots, y[T]]$ is used to construct a sequence of statistics $a_K[0], a_K[1], \dots, a_K[T]$, whose empirical distribution should be approximately uniform if $\tilde{p}_{t,\theta} \approx p_t$ for $t = 0, \dots, T$, where $\tilde{p}_{t,\theta}$ is the pdf of the output r.v. $\tilde{y}[t] = g_\theta(z_t, \mathbf{h}[t])$. To build the ISL, we follow the same procedure described in Section 2 to obtain a differentiable surrogate.

5.2. Multivariate time series prediction

For a multivariate time series the data has the form $\mathbf{y} = [\mathbf{y}[0], \dots, \mathbf{y}[T]]$ where each element of the series is an N -dimensional vector, i.e., $\mathbf{y}[t] = [y_1[t], \dots, y_N[t]]^\top$. A NN $g_\theta(\cdot, \mathbf{h}[t])$ can be trained using the same scheme as in Figure 7 and an ISL loss function constructed from the N marginals $p(y_i[t]|\mathbf{y}[0], \dots, \mathbf{y}[t-1])$, as suggested in [1], or using the ISL-slicing (Algorithm 2) method introduced in Section 4.

5.3. Experiments

This subsection presents the results of multivariate long-sequence time-series forecasting on the ETTh2, ETTm1, and ETTm2 datasets using Autoformer and various ISL-based methods. The Electricity Transformer Temperature (ETT) dataset comprises four distinct subsets: two with hourly resolutions (ETTh) and two with 15-minute resolutions (ETTM), each containing seven features related to oil and load characteristics of electricity transformers collected between July 2016 and July 2018. For more details on the methods and datasets, refer to [37]. The evaluation spans multiple forecasting horizons (τ) and is assessed using two key metrics: mean squared error (MSE) and mean absolute error (MAE). Detailed results are provided in Table 8.

For these experiments, we use a 1-layer RNN with 5 units, followed by batch normalization and a 2-layer MLP with 10 units per layer. The MLP has ReLU in the first layer, identity activation in the last, and 5% dropout in the first layer. Despite this simple architecture, ISL outperforms state-of-the-art transformers. We also observe that the ISL-slicing method generally performs better than both the marginal fitting technique and other state-of-the-art methods, with improvements as the number of projections increases. Notably, the ISL models (with $\approx 25K$ parameters), using an RNN and a simple MLP, achieves better forecasting accuracy than many transformer models with millions of parameters [37].

DB	τ	Autoformer		ISL-M		ISL-S7		ISL-S10		ISL-S20	
		MSE	MAE	MSE	MAE	MSE	MAE	MSE	MAE	MSE	MAE
ETTh2	96	0.358	0.397	0.305	0.435	0.305	0.453	0.275	0.433	0.264	0.405
	192	0.456	0.452	0.449	0.525	0.606	0.636	0.542	0.573	0.547	0.604
	336	0.482	0.486	0.410	0.511	0.413	0.547	0.330	0.426	0.444	0.508
	720	0.515	0.511	0.400	0.499	0.751	0.684	0.557	0.574	0.648	0.644
ETTM1	96	0.672	0.571	0.408	0.508	0.427	0.551	0.284	0.434	0.192	0.374
	192	0.795	0.669	0.573	0.623	0.665	0.651	0.347	0.499	0.359	0.487
	336	1.212	0.871	0.702	0.670	0.786	0.777	0.673	0.682	0.537	0.610
	720	1.166	0.823	0.768	0.686	0.915	0.728	0.869	0.773	0.755	0.738
ETTM2	96	0.255	0.339	0.276	0.443	0.211	0.376	0.220	0.370	0.223	0.358
	192	0.281	0.340	0.335	0.463	0.328	0.429	0.260	0.395	0.213	0.354
	336	0.339	0.372	0.305	0.455	0.360	0.474	0.305	0.454	0.149	0.310
	720	0.433	0.432	0.427	0.546	0.372	0.501	0.363	0.492	0.240	0.397

Table 8: Forecasting results for multivariate time-series on ETTh2, ETTm1, and ETTm2 datasets using Autoformer and ISL. ISL-M denotes the marginal approach, and ISL-S n is the ISL-slicing with n random projections.

6. Conclusions

We have investigated the construction of loss functions based on rank statistics with an invariant distribution in order to train implicit generative models that can reproduce heavy-tailed and multivariate data distributions. As a result, we have introduced two novel methodologies, Pareto-ISL and ISL-slicing. Pareto-ISL is used to fit a NN with a Pareto-distributed random input. The resulting model can represent accurately both the

central features and the tails of heavy-tailed data distributions. ISL-slicing can be used to train NN with a random input and a high-dimensional output. We have shown through simulations with several data sets (including time series data) that the proposed methods are competitive with (and often outperform) state of the art models. The computational cost of training generative models with ISL-based methods is usually low compared to the state of the art schemes.

7. Acknowledgements

This work has been partially supported by the Office of Naval Research (award N00014-22-1-2647) and Spain’s Agencia Estatal de Investigación (ref. PID2021-125159NB-I00 TYCHE and PID2021-123182OB-I00 EPiCENTER) funded by MCIN/AEI/10.13039/501100011033 and by “ERDF A way of making Europe”. Pablo M. Olmos also acknowledges the support by BBVA Foundation (*Beca Leonardo a Investigadores y Creadores Culturales 2024*) and by the Comunidad de Madrid under grants IND2022/TIC-23550 and ELLIS Unit Madrid.

Appendix A. Proof of Theorem 2

For clarity, we introduce the following notation: for a real function $f : \mathbb{R} \rightarrow \mathbb{R}$ and the pdf p of a univariate r.v. we define

$$(f, p) := \int_{\mathbb{R}} f(x)p(x) dx.$$

Let $B_1(\mathbb{R}) := \{f : \mathbb{R} \rightarrow \mathbb{R} \mid \sup_{x \in \mathbb{R}} |f(x)| \leq 1\}$ be the set of real functions bounded by 1. We note that the assumption $\sup_{f \in B_1(\mathbb{R})} |(f, p) - (f, \tilde{p})|$ in [1, Theorem 2] is equivalent to the assumption of Theorem 3. Indeed,

$$\begin{aligned} \|p - \tilde{p}\|_{L^1(\mathbb{R})} &= \int_{\mathbb{R}} |p(x) - \tilde{p}(x)| dx = \int_{\mathbb{R}} \text{sgn}(p(x) - \tilde{p}(x))(p(x) - \tilde{p}(x)) dx \\ &= \sup_{f \in B_1(\mathbb{R})} |(f, p) - (f, \tilde{p})|. \end{aligned}$$

The remainder of the proof follows directly from [1, Theorem 2]. \square

Appendix B. Proof of Theorem 4

Appendix B.1. Preliminary results

Let, $\tilde{F}_\theta(y_0)$ represents the cdf of the transformed r.v. $y = g_\theta(z)$, evaluated at y_0 , where g_θ is a function parameterized by θ . The r.v. y has a pdf denoted \tilde{p}_θ and $z \sim p_z$.

Let $\tilde{y}_1, \dots, \tilde{y}_K$ be K iid draws from \tilde{p}_θ . Using $\tilde{F}_\theta(y_0)$, we define the probability of observing exactly n successes in K independent Bernoulli trials. The i -th trial is

considered a success when $\tilde{y}_i \leq y_0$, hence the success probability is $\tilde{F}_\theta(y_0)$. We write of the resulting binomial distribution as

$$h_{n,\theta}(y_0) = \binom{K}{n} [\tilde{F}_\theta(y_0)]^n [1 - \tilde{F}_\theta(y_0)]^{K-n}, \quad \text{for } n \in \{0, \dots, K\}. \quad (\text{B.1})$$

Using B.1, the pmf of the rank statistic $A_K = \left| \left\{ \tilde{y} \in \{\tilde{y}_i\}_{i=1}^K : \tilde{y} \leq y_0 \right\} \right|$ when $y_0 \sim \tilde{p}_\theta$ can be constructed as

$$\mathbb{Q}_{K,\tilde{p}_\theta}(n) = \int_{\mathbb{R}} h_{n,\theta}(y) \tilde{p}_\theta(y) dy, \quad \text{for } n \in \{0, \dots, K\}. \quad (\text{B.2})$$

Lemma 1. *The cdf $\tilde{F}_\theta(y_0) = \mathbb{P}(g_\theta(z) \leq y_0)$ is continuous in θ , for every fixed $y_0 \in \mathbb{R}$.*

Proof. The cdf $\tilde{F}_\theta(y_0)$ can be expressed as

$$\tilde{F}_\theta(y_0) = \mathbb{P}(y \leq y_0) = \mathbb{P}(g_\theta(z) \leq y_0) = \int_{\mathbb{R}} \mathbb{I}_{S_{y_0,\theta}}(z) p_z(z) dz,$$

where p_z is the pdf of the input noise, $S_{y_0,\theta} = \{u \in \mathbb{R} : g_\theta(u) \leq y_0\}$ and $\mathbb{I}_{S_{y_0,\theta}}(z)$ is the indicator function. We need to prove that for any sequence $\{\theta_m\}_{m=1}^\infty$ such that $\theta_m \rightarrow \theta$ as $m \rightarrow \infty$, we have $\lim_{m \rightarrow \infty} |\tilde{F}_{\theta_m}(y_0) - \tilde{F}_\theta(y_0)| = 0$. We can write

$$|\tilde{F}_{\theta_m}(y_0) - \tilde{F}_\theta(y_0)| \leq \int_{\mathbb{R}} |\mathbb{I}_{S_{y_0,\theta_m}}(z) - \mathbb{I}_{S_{y_0,\theta}}(z)| p_z(z) dz.$$

If we define the set $A_m = \{u \in \mathbb{R} : (g_\theta(u) \leq y_0 < g_{\theta_m}(u)) \text{ or } (g_{\theta_m}(u) \leq y_0 < g_\theta(u))\}$ then is clear that

$$|\mathbb{I}_{S_{y_0,\theta_m}}(z) - \mathbb{I}_{S_{y_0,\theta}}(z)| = \begin{cases} 1 & \text{if } z \in A_m, \\ 0 & \text{otherwise.} \end{cases}$$

Hence, we can write

$$|\tilde{F}_{\theta_m}(y_0) - \tilde{F}_\theta(y_0)| = \int_{\mathbb{R}} \mathbb{I}_{A_m}(z) p_z(z) dz = \int_{A_m} p_z(z) dz, \quad (\text{B.3})$$

and there is a constant $C < \infty$ such that $\int_{A_m} p_z dz \leq C \int_{A_m} dz$. However $g_\theta(z)$ is continuous in θ for almost every $z \in \mathbb{R}$, i.e., $\lim_{m \rightarrow \infty} g_{\theta_m}(z) = g_\theta(z)$, which implies that $\lim_{m \rightarrow \infty} \int_{A_m} dz = 0$. Therefore $\lim_{m \rightarrow \infty} |\tilde{F}_{\theta_m}(y_0) - \tilde{F}_\theta(y_0)| \leq C \int_{A_m} dz = 0$. \square

Lemma 2. *For each $n \in \{0, 1, \dots, K\}$, there is a constant $C_{n,K} < \infty$ such that*

$$|h_{n,\theta}(y_0) - h_{n,\theta'}(y_0)| \leq \binom{K}{n} C_{n,K} |\tilde{F}_\theta(y_0) - \tilde{F}_{\theta'}(y_0)|.$$

Proof. We can bound the difference between $h_{n,\theta}(y_0)$ and $h_{n,\theta'}(y_0)$ using B.1 as

$$|h_{n,\theta}(y_0) - h_{n,\theta'}(y_0)| \leq \binom{K}{n} |\tilde{F}_\theta(y_0)^n (1 - \tilde{F}_\theta(y_0))^{K-n} - \tilde{F}_{\theta'}(y_0)^n (1 - \tilde{F}_{\theta'}(y_0))^{K-n}|.$$

Let us define $f(q) = q^n(1-q)^{K-n}$, which is continuously differentiable for $q \in [0, 1]$. By the mean value theorem, for some value $\tilde{F}_{\theta^*}(y_0) \in [\tilde{F}_\theta(y_0) \wedge \tilde{F}_{\theta'}(y_0), \tilde{F}_\theta(y_0) \vee \tilde{F}_{\theta'}(y_0)]$, we have

$$|f(\tilde{F}_\theta(y_0)) - f(\tilde{F}_{\theta'}(y_0))| \leq |f'(\tilde{F}_{\theta^*}(y_0))| |\tilde{F}_\theta(y_0) - \tilde{F}_{\theta'}(y_0)|.$$

Since $f(q) = q^n(1-q)^{K-n}$ is a polynomial in q , its derivative $f'(q)$ is continuous and bounded on the interval $q \in [0, 1]$. Given that $\tilde{F}_{\theta^*}(y_0) \in [0, 1]$ (as it is a cdf), there exists a constant C_n such that, $|f'(\tilde{F}_{\theta^*}(y_0))| \leq C_n$ for any $\tilde{F}_{\theta^*}(y_0)$. \square

Lemma 3. *Let $\tilde{F}_\theta(y_0)$ and $\tilde{F}_{\theta'}(y_0)$ be the cdfs of the transformed r.v.s $y = g_\theta(z)$ and $y' = g_{\theta'}(z)$, respectively, where $g_\theta(z)$ is differentiable w.r.t. z and satisfies the Lipschitz condition $|g_\theta(z) - g_{\theta'}(z)| \leq L_{\max} \|\theta - \theta'\|$ for some Lipschitz constant $L_{\max} < \infty$, and there exists $m > 0$ such that $\inf_{(z,\theta)} |g'_\theta(z)| \geq m$. Then*

$$|\tilde{F}_\theta(y_0) - \tilde{F}_{\theta'}(y_0)| \leq L_1 \|\theta - \theta'\|,$$

where $L_1 = \|p_z\|_{L^\infty(\mathbb{R})} \frac{2L_{\max}}{m}$ and $p_z(z)$ is the pdf of the input variable z .

Proof. Let $A = \{u \in \mathbb{R} : (g_\theta(u) \leq y_0 < g_{\theta'}(u)) \text{ or } (g_{\theta'}(u) \leq y_0 < g_\theta(u))\}$. By the same argument as in the proof of Lemma 1 (see Eq. B.3) we have

$$|\tilde{F}_\theta(y_0) - \tilde{F}_{\theta'}(y_0)| \leq \int_A p_z(z) dz. \quad (\text{B.4})$$

We now prove that $A \subseteq B = \left\{u \in \mathbb{R} \mid |g_\theta(u) - y_0| \leq L_{\max} \|\theta - \theta'\|\right\}$. For any $z \in A$, there are two possible cases to consider: either $g_\theta(z) \leq y_0 < g_{\theta'}(z)$ or $g_{\theta'}(z) \leq y_0 < g_\theta(z)$. In the first case, we can see that $|g_\theta(z) - y_0| \leq |g_\theta(z) - g_{\theta'}(z)| \leq L_{\max} \|\theta - \theta'\|$ by the Lipschitz assumption. An analogous argument holds for the second case. Thus, we have shown that for any $z \in A$, $|g_\theta(z) - y_0| \leq L_{\max} \|\theta - \theta'\|$ and, therefore, $A \subseteq B$.

Next, we estimate the Lebesgue measure $\mathcal{L}(B)$ of the set B . By assumption, $g_\theta(z)$ is differentiable w.r.t. z , with $\inf_{(z,\theta) \in \mathcal{Z} \times \mathbb{R}^d} |g'_\theta(z)| \geq m > 0$. Hence, we can perform a change of variable $y = g_\theta(z)$, and obtain $z = g_\theta^{-1}(y)$, where g_θ^{-1} is the local inverse function. We note that $z \in B$ when $y \in [y_0 - \delta, y_0 + \delta]$, where $\delta = L_{\max} \|\theta - \theta'\|$. The Lebesgue measure of B can be upper bounded as

$$\mathcal{L}(B) = \int_B dz \leq \int_{y_0 - \delta}^{y_0 + \delta} \left| \frac{dz}{dy} \right| dy \leq \frac{1}{m} \int_{y_0 - \delta}^{y_0 + \delta} dy = \frac{2\delta}{m} = \frac{2L_{\max}}{m} \|\theta - \theta'\|,$$

since $\frac{dz}{dy} = \frac{1}{g'_\theta(z)}$ and, by assumption, $\inf_{(z,\theta)} |g'_\theta(z)| \geq m$, hence $\left| \frac{dz}{dy} \right| = \frac{1}{|g'_\theta(z)|} \leq \frac{1}{m}$.

Finally, we proceed to bound the absolute difference between the cdfs. In particular,

$$|\tilde{F}_\theta(y_0) - \tilde{F}_{\theta'}(y_0)| \leq \int_A p_z(z) dz \leq \int_B p_z(z) dz \leq \|p_z\|_{L^\infty(\mathbb{R})} \mathcal{L}(B) \leq L_1 \|\theta - \theta'\|,$$

the first inequality follows from B.4, the second is given by $A \subseteq B$, and the last inequality follow from the upper bound on $\mathcal{L}(B)$ with $L_1 = \|p_z\|_{L^\infty(\mathbb{R})} \frac{2L_{\max}}{m}$. \square

Appendix B.2. Proof of Theorem 4

Part 1. To prove that $d_K(p, \tilde{p}_\theta)$ is continuous w.r.t. θ , we need to show that

$$\lim_{m \rightarrow \infty} |d_K(p, \tilde{p}_{\theta_m}) - d_K(p, \tilde{p}_\theta)| = 0$$

for any sequence $\{\theta_m\}_{m=1}^\infty$ such that $\theta_m \rightarrow \theta$.

We begin by examining the difference $|d_K(p, \tilde{p}_{\theta_m}) - d_K(p, \tilde{p}_\theta)|$. Let us denote $\mathbf{q}_{K, \tilde{p}_\theta} = [\mathbb{Q}_{K, \tilde{p}_\theta}(0), \dots, \mathbb{Q}_{K, \tilde{p}_\theta}(K)]^\top$. We readily arrive at the bound

$$\begin{aligned} |d_K(p, \tilde{p}_{\theta_m}) - d_K(p, \tilde{p}_\theta)| &= \frac{1}{K+1} \left\| \frac{1}{K+1} \mathbf{1}_{K+1} - \mathbf{q}_{K, \tilde{p}_{\theta_m}} \right\|_{\ell_1} - \left\| \frac{1}{K+1} \mathbf{1}_{K+1} - \mathbf{q}_{K, \tilde{p}_\theta} \right\|_{\ell_1} \\ &\leq \frac{1}{K+1} \|\mathbf{q}_{K, \tilde{p}_{\theta_m}} - \mathbf{q}_{K, \tilde{p}_\theta}\|_{\ell_1} \\ &\leq \frac{1}{K+1} \sum_{n=0}^K \int_{\mathbb{R}} |h_{n, \theta_m}(y) - h_{n, \theta}(y)| \max\{\tilde{p}_{\theta_m}(y), \tilde{p}_\theta(y)\} dy, \end{aligned} \quad (\text{B.5})$$

where (B.5) follows from the reverse triangle inequality and (B.6) is obtained from the construction of the pmf $\mathbb{Q}_{K, \tilde{p}_\theta}(n)$ in Eq. (B.2). It is easy to see that

$$|h_{n, \theta_m}(y) - h_{n, \theta}(y)| \max\{\tilde{p}_{\theta_m}(y), \tilde{p}_\theta(y)\} \leq 2(\tilde{p}_\theta(y) + \tilde{p}_{\theta_m}(y)),$$

hence the dominated convergence theorem yields

$$\lim_{m \rightarrow \infty} |d_K(p, \tilde{p}_{\theta_m}) - d_K(p, \tilde{p}_\theta)| \leq \sum_{n=0}^K \int_{\mathbb{R}} \lim_{m \rightarrow \infty} |h_{n, \theta_m}(y) - h_{n, \theta}(y)| \max\{\tilde{p}_{\theta_m}(y), \tilde{p}_\theta(y)\} dy. \quad (\text{B.7})$$

However, $h_{n, \theta_m}(y)$ is continuous in θ because it depends continuously on the cdf $\tilde{F}_{\theta_m}(y)$ which, in turn, is continuous by Lemma 1. Therefore,

$$\lim_{m \rightarrow \infty} |h_{n, \theta_m}(y) - h_{n, \theta}(y)| = 0 \quad (\text{B.8})$$

for any sequence $\{\theta_m\}_{m=1}^\infty$ such that $\theta_m \rightarrow \theta$. Combining (B.8) with the inequality (B.7) yields $\lim_{m \rightarrow \infty} |d_K(p, \tilde{p}_{\theta_m}) - d_K(p, \tilde{p}_\theta)| = 0$ whenever $\theta_m \rightarrow \theta$ and completes the proof of Part 1. \square

Part 2. By Rademacher’s theorem (see [19, Theorem 3.2]), if $d_K(p, \tilde{p}_\theta)$ is Lipschitz then it is differentiable almost everywhere. Hence, we aim to prove that $d_K(p, \tilde{p}_\theta)$ is Lipschitz continuous w.r.t. θ .

Lemma 2 yields the upper bound

$$|h_{n,\theta}(y_0) - h_{n,\theta'}(y_0)| \leq \binom{K}{n} C_{n,K} |\tilde{F}_\theta(y_0) - \tilde{F}_{\theta'}(y_0)|, \quad (\text{B.9})$$

where $C_{n,K} < \infty$ is a constant that depends on n and K . Combining (B.9) with Lemma 3 yields the Lipschitz continuity of $h_{n,\theta}(y_0)$, namely

$$|h_{n,\theta}(y_0) - h_{n,\theta'}(y_0)| \leq \binom{K}{n} C_{n,K} L_1 \|\theta - \theta'\|, \quad (\text{B.10})$$

where $L_1 < \infty$ is a constant. Moreover, we have a bound for the pdf \tilde{p}_θ of the form

$$\sup_{\theta,y} \tilde{p}_\theta(y) = \sup_{\theta,y} \frac{p_z(g_\theta^{-1}(y))}{|g'_\theta(g_\theta^{-1}(y))|} \leq \frac{\|p_z\|_{L^\infty(\mathbb{R})}}{m}, \quad (\text{B.11})$$

where $g_\theta^{-1}(y)$ is the local inverse of $g_\theta(y)$ and we have used the assumption $\inf_{z,\theta} |g'_\theta(z)| \geq m > 0$. Substituting the upper bounds (B.10) and (B.11) back into (B.6) (with $\theta_m = \theta'$) yields

$$|d_K(p, \tilde{p}_\theta) - d_K(p, \tilde{p}_{\theta'})| \leq \frac{1}{K+1} \frac{\|p_z\|_{L^\infty(\mathbb{R})}}{m} \sum_{n=0}^K \binom{K}{n} C_{n,K} L_1 \|\theta - \theta'\|.$$

Finally, we note that $\sum_{n=0}^K \binom{K}{n} = 2^K$ to obtain

$$|d_K(p, \tilde{p}_\theta) - d_K(p, \tilde{p}_{\theta'})| \leq \frac{\|p_z\|_{L^\infty(\mathbb{R})}}{m(K+1)} 2^K \left(\max_{0 \leq n \leq K} C_{n,K} \right) L_1 \|\theta - \theta'\|.$$

and complete the proof. \square

Appendix C. Experimental results

Appendix C.1. Comparison of the surrogate and theoretical loss functions

Table C.9 compares the error rates between the surrogate and theoretical losses. The metrics displayed include the L_1 and L_∞ norms of the values obtained from the surrogate loss and the theoretical loss at each epoch, along with their respective percentage errors. In this setup the noise is drawn from a standard Gaussian, $\mathcal{N}(0, 1)$, the number of training epochs is 1000, $K = 10$, the sample size is $N = 1000$, and the results are averaged over 100 trials. The final three rows in the table describe mixture models with equal component weights: Model 1 is a mixture of $\mathcal{N}(5, 2)$ and $\mathcal{N}(-1, 1)$, Model 2 is a mixture of $\mathcal{N}(5, 2)$, $\mathcal{N}(-1, 1)$, and $\mathcal{N}(-10, 3)$, and Model 3 is a mixture of $\mathcal{N}(-5, 2)$ and Pareto(5, 1).

Target	L_1	L_∞	% error L_1	% error L_∞
$\mathcal{N}(4, 2)$	0.005307 ± 0.001505	0.254805 ± 0.034452	0.019625	0.930903
$\mathcal{U}(-2, 2)$	0.015454 ± 0.001450	0.244568 ± 0.028237	0.015454	0.734944
Cauchy(1, 2)	0.005192 ± 0.001329	0.242361 ± 0.028494	0.015636	0.729832
Pareto(1, 1)	0.003290 ± 0.004527	0.137377 ± 0.183803	0.000547	0.022837
Model ₁	0.004701 ± 0.002198	0.175290 ± 0.025778	0.003925	1.471159
Model ₂	0.004991 ± 0.001895	0.173241 ± 0.030297	0.033870	0.117551
Model ₃	0.009817 ± 0.002167	0.348440 ± 0.068293	0.016706	0.592932

Table C.9: Comparison of error between the surrogate and theoretical losses. Noise is $\sim \mathcal{N}(0, 1)$, $K = 10$, epochs = 1000, and $N = 1000$. Values obtained are the average of 100 trials, and the corresponding standard deviations are also indicated.

Figure C.8 illustrates the surrogate loss versus the theoretical one across several distributions, presented in log-scale to highlight performance differences.

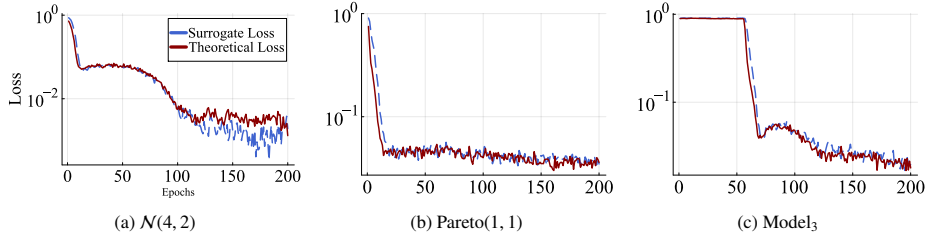


Figure C.8: Comparison of the surrogate loss and the theoretical one during training for different distributions. Only the first 200 epochs are shown, and the scale in the vertical axis is logarithmic.

In conclusion, the surrogate loss performs well for different target distributions, as shown in Table C.9 and Figure C.8. The small L_1 and L_∞ norms with minimal percentage errors indicate its close approximation of the theoretical loss. Even for complex distributions like the mixture models, it maintains low error rates, demonstrating robustness and reliability.

Appendix C.2. Efficiency gains from progressive K Training vs. fixed K

In Table C.10, we compare the outcomes of progressively increasing K during training against a fixed K value. After running 100 trials and averaging the results, we found that progressively increasing K reduces training time by up to 50% without sacrificing accuracy. Additionally, the KSD values are comparable or slightly better, indicating that this strategy offers a more efficient balance between time savings and model performance.

Appendix C.3. Comparing ISL and Pareto-ISL for Approximating Heavy-Tailed Multi-Dimensional Distributions

We define multidimensional distributions with heavy-tailed characteristics and train a generator to approximate them. Specifically, we introduce a joint distribution on

	Progressively K		$K = 10$		Impr. %
	KSD	Time	KSD	Time	Time
$\mathcal{N}(4, 2)$	0.00831 ± 0.00268	4149	0.00894 ± 0.00276	9016	53.98%
$\mathcal{U}(-2, 2)$	0.01431 ± 0.00158	8721	0.01373 ± 0.00152	11745	25.74%
Cauchy(1, 2)	0.01084 ± 0.00146	3700	0.01190 ± 0.00161	8002	53.76%
Pareto(1, 1)	0.08344 ± 0.00334	4978	0.24238 ± 0.17257	10800	53.90%
Model ₁	0.01001 ± 0.00134	8000	0.01175 ± 0.00336	11044	27.56%
Model ₂	0.01067 ± 0.00270	11042	0.00921 ± 0.00187	8039	-27.19%
Model ₃	0.18525 ± 0.00406	8700	0.18053 ± 0.04512	11207	22.37%

Table C.10: Comparison of progressively training by increasing K with fixed K under the hyperparameters: Noise $\sim \mathcal{N}(0, 1)$, $K_{\max} = 10$ (progressive only), epochs = 200, and $N = 1000$.

$[X_0, X_1]$ with the following component definitions

$$X_0 = A + B, \quad X_1 = \text{sign}(A - B) |A - B|^{1/2},$$

where A and B are independent Cauchy r.v.s. with location 0.5 and scale 1.0. Note that X_0 and X_1 have different tail indices (1 and 1/2, respectively) and are not independent.

We trained a Pareto-ISL model on this distribution using a NN with an input layer of 2 features, followed by three hidden layers of 256 neurons each with ReLU activations. The input was a mixture of GPD with tail indices of 1 and 0.5. As shown in Figure C.9, the marginals and joint distributions closely match the target. We also compared these results to those obtained using ISL with multivariate normal input noise, characterized by a zero mean and identity covariance matrix.

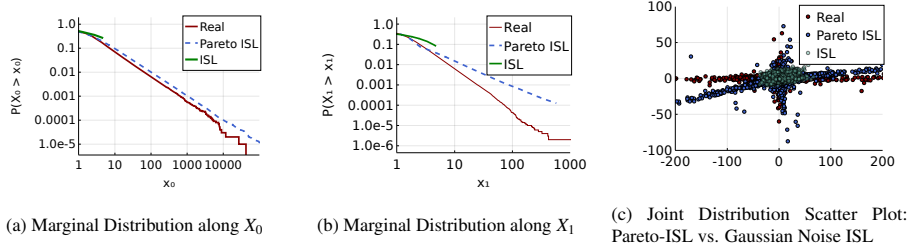


Figure C.9: Plots (a) and (b) show the marginal distributions along the X_0 and X_1 axes for the Pareto-ISL model and ISL with Gaussian noise. Plot (c) presents a scatter plot of 10000 samples from both models, illustrating the joint distribution between the two dimensions.

References

- [1] J. M. de Frutos, P. Olmos, M. A. Vázquez, J. Míguez, Training implicit generative models via an invariant statistical loss, in: International Conference on Artificial Intelligence and Statistics, PMLR, 2024, pp. 2026–2034.
- [2] P. J. Diggle, R. J. Gratton, Monte carlo methods of inference for implicit statistical

- models, *Journal of the Royal Statistical Society Series B: Statistical Methodology* 46 (2) (1984) 193–212.
- [3] D. P. Kingma, M. Welling, et al., An introduction to variational autoencoders, *Foundations and Trends® in Machine Learning* 12 (4) (2019) 307–392.
 - [4] Y. Deng, W. Byrne, Hmm word and phrase alignment for statistical machine translation, *IEEE Transactions on Audio, Speech, and Language Processing* 16 (3) (2008) 494–507.
 - [5] Y. Ding, L.-P. Tian, X. Lei, B. Liao, F.-X. Wu, Variational graph auto-encoders for mirna-disease association prediction, *Methods* 192 (2021) 25–34.
 - [6] S. Mohamed, B. Lakshminarayanan, Learning in implicit generative models, *arXiv preprint arXiv:1610.03483* (2016).
 - [7] A. Chorin, M. Morzfeld, X. Tu, Implicit particle filters for data assimilation, *Communications in Applied Mathematics and Computational Science* 5 (2) (2010) 221–240.
 - [8] M. Morzfeld, A. J. Chorin, Implicit particle filtering for models with partial noise, and an application to geomagnetic data assimilation, *Nonlinear Processes in Geophysics* 19 (3) (2012) 365–382.
 - [9] B. Weir, R. N. Miller, Y. H. Spitz, Implicit estimation of ecological model parameters, *Bulletin of mathematical biology* 75 (2013) 223–257.
 - [10] D. Tran, R. Ranganath, D. Blei, Hierarchical implicit models and likelihood-free variational inference, *Advances in Neural Information Processing Systems* 30 (2017).
 - [11] V. Puzyrev, T. Salles, G. Surma, C. Elders, Geophysical model generation with generative adversarial networks, *Geoscience Letters* 9 (1) (2022) 32.
 - [12] V. Elvira, J. Míguez, P. M. Djurić, On the performance of particle filters with adaptive number of particles, *Statistics and Computing* 31 (2021) 1–18.
 - [13] M. Rosenblatt, Remarks on a multivariate transformation, *The annals of mathematical statistics* 23 (3) (1952) 470–472.
 - [14] P. M. Djuric, J. Míguez, Assessment of nonlinear dynamic models by kolmogorov–smirnov statistics, *IEEE transactions on signal processing* 58 (10) (2010) 5069–5079.
 - [15] H. Brezis, H. Brézis, *Functional analysis, Sobolev spaces and partial differential equations*, Vol. 2, Springer, 2011.
 - [16] Z. Chen, M. Katsoulakis, L. Rey-Bellet, W. Zhu, Sample complexity of probability divergences under group symmetry, in: *International Conference on Machine Learning*, PMLR, 2023, pp. 4713–4734.

- [17] M. Sugiyama, S. Liu, M. C. du Plessis, M. Yamanaka, M. Yamada, T. Suzuki, T. Kanamori, Direct divergence approximation between probability distributions and its applications in machine learning, *Journal of Computing Science and Engineering* 7 (2) (2013) 99–111.
- [18] T. Huster, J. Cohen, Z. Lin, K. Chan, C. Kamhoua, N. O. Leslie, C.-Y. J. Chiang, V. Sekar, Pareto gan: Extending the representational power of gans to heavy-tailed distributions, in: *International Conference on Machine Learning*, PMLR, 2021, pp. 4523–4532.
- [19] L. Evans, *Measure theory and fine properties of functions*, Routledge, 2018.
- [20] R. Arora, A. Basu, P. Mianjy, A. Mukherjee, Understanding deep neural networks with rectified linear units, *arXiv preprint arXiv:1611.01491* (2016).
- [21] S. Resnick, C. Stărică, Smoothing the hill estimator, *Advances in Applied Probability* 29 (1) (1997) 271–293.
- [22] A. A. Balkema, L. De Haan, Residual life time at great age, *The Annals of probability* 2 (5) (1974) 792–804.
- [23] M. Arjovsky, S. Chintala, L. Bottou, Wasserstein generative adversarial networks, in: *International conference on machine learning*, PMLR, 2017, pp. 214–223.
- [24] C.-L. Li, W.-C. Chang, Y. Cheng, Y. Yang, B. Póczos, MMD GAN: Towards deeper understanding of moment matching network, *Advances in neural information processing systems* 30 (2017).
- [25] N. Bonneel, J. Rabin, G. Peyré, H. Pfister, Sliced and radon wasserstein barycenters of measures, *Journal of Mathematical Imaging and Vision* 51 (2015) 22–45.
- [26] S. Kolouri, K. Nadjahi, U. Simsekli, R. Badeau, G. Rohde, Generalized sliced wasserstein distances, *Advances in neural information processing systems* 32 (2019).
- [27] A. N. Gorban, I. Y. Tyukin, Blessing of dimensionality: mathematical foundations of the statistical physics of data, *Philosophical Transactions of the Royal Society A: Mathematical, Physical and Engineering Sciences* 376 (2118) (2018) 20170237.
- [28] Y. Saatci, A. G. Wilson, Bayesian gan, *Advances in neural information processing systems* 30 (2017).
- [29] L. Dinh, J. Sohl-Dickstein, S. Bengio, Density estimation using real nvp, *arXiv preprint arXiv:1605.08803* (2016).
- [30] V. Stimper, D. Liu, A. Campbell, V. Berenz, L. Ryll, B. Schölkopf, J. M. Hernández-Lobato, normflows: A pytorch package for normalizing flows, *Journal of Open Source Software* 8 (86) (2023) 5361. doi:10.21105/joss.05361. URL <https://doi.org/10.21105/joss.05361>

- [31] Y. Luo, Z. Yang, Dyngan: Solving mode collapse in GANs with dynamic clustering, *IEEE Transactions on Pattern Analysis and Machine Intelligence* (2024).
- [32] C. Xiao, P. Zhong, C. Zheng, Bourgan: Generative networks with metric embeddings, *Advances in neural information processing systems* 31 (2018).
- [33] I. Goodfellow, J. Pouget-Abadie, M. Mirza, B. Xu, D. Warde-Farley, S. Ozair, A. Courville, Y. Bengio, Generative adversarial nets, *Advances in neural information processing systems* 27 (2014).
- [34] A. Srivastava, L. Valkov, C. Russell, M. U. Gutmann, C. Sutton, Veegan: Reducing mode collapse in GANs using implicit variational learning, *Advances in neural information processing systems* 30 (2017).
- [35] P. Zhong, Y. Mo, C. Xiao, P. Chen, C. Zheng, Rethinking generative mode coverage: A pointwise guaranteed approach, *Advances in Neural Information Processing Systems* 32 (2019).
- [36] A. Radford, L. Metz, S. Chintala, Unsupervised representation learning with deep convolutional generative adversarial networks, *arXiv preprint arXiv:1511.06434* (2015).
- [37] A. Zeng, M. Chen, L. Zhang, Q. Xu, Are transformers effective for time series forecasting?, in: *Proceedings of the AAAI conference on artificial intelligence*, Vol. 37, 2023, pp. 11121–11128.